Applied Physics Express

Coaxial heterostructure formation of highly crystalline graphene flakes on boron nitride nanotubes by high-temperature chemical vapor deposition

To cite this article before publication: Masakiyo Kato *et al* 2023 *Appl. Phys. Express* in press https://doi.org/10.35848/1882-0786/acbd0e

Template for APEX (Mar. 2022)

Coaxial heterostructure formation of highly crystalline graphene flakes on boron nitride nanotubes by high-temperature chemical vapor deposition

Masakiyo Kato[1], Taiki Inoue[1]*, Yi Ling Chiew[2], Yungkai Chou[1], Masashi Nakatake[3], Shoichi Takakura[3,4], Yoshio Watanabe[3], Kazu Suenaga[2,5], Yoshihiro Kobayashi[1]

[1]*Department of Applied Physics, Osaka University, Osaka 565-0871, Japan*

[2]*The Institute of Scientific and Industrial Research (ISIR-SANKEN), Osaka University, Osaka 567-0047, Japan*

[3]*Aichi Synchrotron Radiation Center, Aichi Science & Technology Foundation, Aichi 489-0985, Japan*

[4]*Synchrotron Radiation Research Center, Nagoya University, Aichi 464-8603, Japan*

[5]*Nanomaterials Research Institute, National Institute of Advanced Industrial Science and Technology (AIST), Tsukuba 305-8565, Japan*

E-mail: inoue.taiki@ap.eng.osaka-u.ac.jp

We develop a high-temperature chemical vapor deposition of highly crystalline graphene on the surface of boron nitride nanotubes (BNNTs). The growth of few-layer graphene flakes on BNNT templates was confirmed by scanning transmission electron microscopy. Based on an investigation of the effect of growth temperature and growth time on defect density, graphene with a relatively high crystallinity was obtained at 1350 °C. The absence of undesirable alterations in the BNNT lattice during graphene growth was verified by multiple analyses. The high-temperature growth of heterolayers would assist in the advancement of nanodevices that coaxially combine graphene and boron nitride.

Carbon nanotubes (CNTs),[1] boron nitride (BN) nanotubes (BNNTs),[2] and transition metal dichalcogenide nanotubes (TMDNTs)[3] are representative nanotube materials that possess unique properties originating from their quasi-one-dimensional structures. The closed lattice structure without dangling bonds on the nanotube surfaces provides a potential for nested structures of different nanotubes via van der Waals (vdW) force.[4),5] Following the rapid development of vdW heterostructures of two-dimensional layered materials,[6] coaxial heterostructures of nanotube materials, i.e., heteronanotubes, have attracted an increasing attention.[7] A controlled synthesis of BNNTs and TMDNTs coaxially on single-walled CNTs (SWCNTs) as a template was realized by chemical vapor deposition (CVD).[7] The ternary heteronanotubes function well as a diode based on semiconductor–insulator–semiconductor junctions.[8] By controllably combining nanotubes with different elements and properties, various electronic and optical functionalities are expected to be integrated into the small body of each heteronanotube. As post-growth manipulation is not readily applicable to nest nanotubes, in contrast to the transfer techniques used for layered vdW heterostructures,[6] development of a direct heterolayer growth is strongly demanded to obtain heteronanotubes.[9]

As CNTs are semiconducting or metallic depending on their atomic structures,[10] they have the potential to be versatile components in heteronanotube devices not only as inner walls[7),8] but also as outer walls. While non-carbon nanotubes have been grown on the outsides of SWCNTs[7),9] and multi-walled CNTs (MWCNTs),[5),11)–13] CNTs have scarcely been synthesized on the outside of non-carbon nanotubes.[14] A few studies have reported growth of outer-wall CNTs, i.e., over-layer graphene, on MWCNT[15] and BNNT[14] templates, but the crystallinity of the obtained graphene is relatively low. Carbon deposition followed by a graphitization treatment can provide a highly crystalline graphene on MWCNTs but is limited to thick graphene layers.[16] Nucleation and growth of single- to few-layer graphene have to be investigated for the application of high-quality thin CNTs as outer walls. Because of the difficulty in employing catalytic metals in coaxial growth, a high growth temperature is preferred to overcome energetic barriers, e.g., for diffusion of precursor carbon adatoms on a template surface and incorporation of the adatoms to graphene at the growth edges.[17),18] Simultaneously, since graphene and BN can form hybridized phases (hexagonal BNC),[19] alteration and atomic substituion[20] of the template structures should be avoided for heterolayer growth at high temperatures.

In this study, we carried out a high-temperature CVD for a synthesis of graphene using BNNT films as a template. The growth of graphene on the surface of BNNTs was evidenced

by scanning transmission electron microscopy (STEM). To obtain a highly crystalline graphene, we analyzed the effects of the growth temperature and growth time. We also characterized the electrical conduction of the graphene-coated BNNT films. The possibility of alteration and atomic substitution of BNNT structures during graphene growth was excluded by vibrational spectroscopy and chemical state analyses.

As a template for graphene growth, suspended BNNT films were prepared. A BNNT powder (BNNT Materials SP10R, diameter of 4 ± 2 nm, wall number of one to five)[21] (~0.2 mg) was lightly dispersed in iso-propanol by stirring over-night,[22] followed by bath sonication for 10 min. BNNT films with a diameter of ~16 mm were formed on filter membranes by vacuum filtration. A graphite sheet (Toyo Tanso PERMA-FOIL, 0.66 mm thick) was processed into a ring structure with an inner diameter of ~8 mm by belt punches and used as a supporting substrate that can withstand a high-temperature process.[23] Note that common substrates such as silicon and quartz are not stable above ~1200 °C. After the membrane filter was dissolved in acetone, the BNNT films floating on the acetone surface were picked up by the ring substrate to obtain a suspended BNNT film on graphite (top optical image in Fig. 1(a)).

Graphene growth by CVD was carried out with an infrared radiation furnace (Thermo Riko SR1800G) where the sample stage was locally heated by a focused infrared light. The temperature of a graphite crucible in which the BNNT sample was placed in the CVD chamber was measured with an infrared thermometer and regarded as the sample temperature. Ethanol was selected as a carbon source because its decomposition provides oxygen atom-containing species, which can assist the efficient growth of nanocarbon materials.[24),25] The growth condition was determined according to previous studies on non-catalytic growth of graphene on graphene templates.[26)–28] After the sample was set in the chamber, and the chamber was pumped down, the temperature was increased to the growth temperature with an Ar flow (100 sccm at ~1150 Pa). The growth temperature was 1150 to 1550 °C. After the sample reached the growth temperature, an ethanol vapor (0.5 sccm) was introduced in addition to Ar (100 sccm), where the total pressure was ~1150 Pa, corresponding to an ethanol partial pressure of ~5.7 Pa. The growth time was 5 to 60 min.

The samples were characterized by STEM-electron energy loss spectroscopy (-EELS) (JEOL ARM200F, acceleration voltage of 60 kV), Raman spectroscopy (HORIBA HR800, excitation wavelength of 532 nm), four-probe sheet resistance measurement (Nittoseiko MCP-T370), Fourier transform infrared (FTIR) spectroscopy (Bruker Hyperion 2000), and X-ray absorption near edge structure (XANES) spectroscopy (BL7U of Aichi Synchrotron

Radiation Center, total fluorescence yield method). For the observation by STEM, the grown samples were lightly dispersed in ethanol and dropped on holey carbon-coated copper grids. Other characterizations were carried out with as-grown film samples.

After the ethanol CVD process, the color of the BNNT films turned from white to black (bottom optical image in Fig. 1(a)), which indicates the growth of carbonaceous materials. A representative STEM image of the sample grown at 1350 °C for 60 min is shown in Fig. 1(b). In addition to amorphous structures, partially crystalized layered structures with an interlayer distance of ~0.35 nm were observed on the surface of nanotubes. The corresponding EELS mapping indicates the strong B and N signals along the continuous tubular structure and C signal from the layered flakes on it (Fig. 1(c)). These observations confirm that few-layer graphene flakes were grown on the surface of the BNNT template.

We investigated the growth temperature dependence of the structure of the graphene grown on the BNNT templates by Raman spectroscopy. Figure 2(a) shows Raman spectra of the samples grown at different temperatures for 5 min. Except for the sample grown at 1550 °C, which exhibits only a broad fluorescence signal, the other samples exhibit Raman signals that are characteristic of graphitic materials. Note that a Raman peak from BNNTs at ~1360 cm^{-1} was not very apparent due to the weak resonance with the excitation laser and the overlap with the fluorescence signal (Fig. S1). The spectra indicate growth of graphene on BNNTs at 1150−1450 °C and absence of graphene growth at 1550 °C under this carbon feeding condition. The lack of graphene growth at 1550 °C can be explained as the density of precursor carbon adatoms on the BNNT surface does not reach the nucleation threshold[18),29)] due to an increase in the desorption rate of adatoms at a high temperature. Another possibility is that the chemical potential of carbon atoms in the gas phase becomes lower than that in the solid phase at high temperature, preventing graphene growth. We observed D, G, D', G', and D+D' bands at approximately 1340, 1590, 1620, 2670, and 2920 cm^{-1}, respectively. The different peak shapes and intensities for each sample reflect the structural change of graphene with the growth temperature.

To compare the crystallinities of graphene on BNNTs, the Raman spectra were analyzed by peak fitting. The areal peak intensity ratio of the D band to the G band, A_D/A_G, (or the corresponding peak height ratio, I_D/I_G) is an indicator of the defect density of graphitic materials.[30)] Note that, whereas A_D/A_G decreases with decreasing defects in the low defect-density region (Stage 1), it exhibits the opposite trend in the high defect-density region (Stage 2).[30)–32)] As the full width at half-maximum (FWHM) peak width of the G band, Γ_G, decreases with decreasing defects rapidly in Stage 2 and gradually in Stage 1,[31),32)] we

focused on Γ_G in addition to A_D/A_G. Figure 2(b) shows A_D/A_G and Γ_G of graphene on BNNTs grown at different temperatures. The order of Γ_G from higher to lower is the samples grown at 1150, 1250, 1450, and 1350 °C, where the latter two possess comparable values. This corresponds to the order of higher defect density. The 1150-°C sample is classified as Stage 2 because it is the most defective but exhibits lower A_D/A_G than some of the other samples. Judging from Γ_G, the 1350- and 1450-°C samples possess lower defect densities than the 1150-°C sample. Other spectral features, such as the peak positions of G band,[31] showed consistent trends (Fig. S2). Since defects in graphene can be classified into edge defects and surface defects, the lower defect density at a higher growth temperature is presumably due to an increased ratio of graphene surface area to defective edge length caused by higher growth rates[17),18)] and/or decreased density of surface defects caused by higher self-healing rates.[33)]

We also investigated the growth time dependence of the graphene crystallinity with a fixed growth temperature of 1350 °C, as shown in Figs. 2(c) and 2(d). The 1350-°C 30-min and 60-min samples are classified as Stage 1 because of the lower Γ_G and A_D/A_G than those of the 1150-°C 5-min sample, which is Stage 2. Thus, the decrease in A_D/A_G with the increase in the growth time represents a decrease in the defect density. This can be attributed to an increased ratio of graphene surface area to edge length caused by the lateral growth of initially nucleated small flakes of graphene with the increase in the growth time. The highest-crystallinity sample grown at 1350 °C for 60 min exhibits a lower D-band intensity (I_D/I_G of 0.59) than those of graphene–BN heterostructures with tubular[14)] and layered[34)] forms obtained at lower growth temperatures in previous studies. The results demonstrate the effectiveness of the high-temperature CVD for highly crystalline heterostructures. Further improvement in crystallinity of graphene is expected with control of carbon feeding rates at high temperatures.

We measured the sheet resistance of the BNNT films before and after the graphene growth. The original BNNT film exhibited a high resistance above the measurement limit ($> 10^6$ Ω/square), confirming the insulating nature of BNNTs. After the graphene growth at 1350 °C for 30 min, the sheet resistance was largely decreased to 110 Ω/square, which indicates the growth of electrically conductive graphene layers.

In addition to the growth of graphene, the preservation of the BNNT lattice structure should be confirmed because the high temperature process may damage the template BNNTs. Figure 3 shows FTIR spectra of the BNNT film samples before and after the graphene growth at 1350 °C for 5 min. While the baseline of the transmittance was decreased after the

growth process due to uniform optical absorption by graphene, the B—N stretching peak at 1370 cm^{-1} and the B—N—B bending peak[23] at 795 cm^{-1} were preserved, suggesting that the BNNT structures are not destroyed during the graphene growth.

To analyze the possible atomic substitution of the BN lattice with C atoms,[19),20)] the chemical states of the samples were analyzed by XANES spectroscopy and EELS. Figure 4(a) shows XANES spectra at the B *K*-edge of a pristine BNNT film and graphene grown on a BNNT film at 1350 °C for 30 min. The almost identical shapes of the two spectra confirm a negligible formation of B—C bonds during the graphene growth at a high temperature. In addition to the large-area measurement by XANES (spot size of ~150 × 50 μm^2), we also analyzed nanometer-scale local chemical states of a BNNT partially covered with graphene by STEM-EELS. Figure 4(b) shows electron energy loss spectra from a bare BNNT area and neighboring graphene-grown area. The graphene on the BNNT exhibits B, C, and N signals, while the bare BNNT area exhibits only B and N signals without a C signal, which indicates the absence of atomic substitution in bare BNNTs even after the graphene growth process. These results support that the obtained heterostructures have an atomically sharp vdW interface without intermixing.

In conclusion, we developed a high-temperature CVD process to synthesize high-quality coaxial heterostructures of graphene and BN. The growth of graphene and preservation of BNNTs were confirmed by microscopic and spectroscopic characterizations. With the analysis of the defect density depending on the growth parameters, we realized graphene with a higher crystallinity than those in previous studies on non-catalytic heterolayer growth. The obtained results pave the way for a controlled formation of nanodevices consisting of highly crystalline graphene–BN heterostructures.

Acknowledgments

A part of this work was supported by JST CREST (JPMJCR20B5), JSPS KAKENHI (JP22K04874 JP21H01763, JP20KK0114, and JP20H00220), Mizuho Foundation for the Promotion of Sciences, and The Murata Science Foundation. A part of this work was conducted at Research Center for Ultra-High Voltage Electron Microscopy, Photonics Center, and Comprehensive Analysis Center, Osaka University. The XANES measurement was conducted at the BL7U of Aichi Synchrotron Radiation Center, Aichi Science & Technology Foundation, Aichi, Japan (Proposal No. 202105044).

References

1) S. Iijima, Nature **354**, 56 (1991).

2) N. G. Chopra, R. J. Luyken, K. Cherrey, V. H. Crespi, M. L. Cohen, S. G. Louie and A. Zettl, Science **269**, 966 (1995).

3) R. Tenne, L. Margulis, M. Genut and G. Hodes, Nature **360**, 444 (1992).

4) K. Suenaga, C. Colliex and N. Demoncy, Science **278**, 653 (1997).

5) W. K. Hsu, Y. Q. Zhu, H. W. Kroto, D. R. M. Walton, R. Kamalakaran and M. Terrones, Appl. Phys. Lett. **77**, 4130 (2000).

6) A. K. Geim and I. V Grigorieva, Nature **499**, 419 (2013).

7) R. Xiang, T. Inoue, Y. Zheng, A. Kumamoto, Y. Qian, Y. Sato, M. Liu, D. Tang, D. Gokhale, J. Guo, K. Hisama, S. Yotsumoto, T. Ogamoto, H. Arai, Y. Kobayashi, H. Zhang, B. Hou, A. Anisimov, M. Maruyama, Y. Miyata, S. Okada, S. Chiashi, Y. Li, J. Kong, E. I. Kauppinen, Y. Ikuhara, K. Suenaga and S. Maruyama, Science **367**, 537 (2020).

8) Y. Feng, H. Li, T. Inoue, S. Chiashi, S. V. Rotkin, R. Xiang and S. Maruyama, ACS Nano **15**, 5600 (2021).

9) Y. Zheng, A. Kumamoto, K. Hisama, K. Otsuka, G. Wickerson, Y. Sato, M. Liu, T. Inoue, S. Chiashi, D.-M. Tang, Q. Zhang, A. Anisimov, E. I. Kauppinen, Y. Li, K. Suenaga, Y. Ikuhara, S. Maruyama and R. Xiang, Proc. Natl. Acad. Sci. **118**, e2107295118 (2021).

10) R. Saito, M. Fujita, G. Dresselhaus and M. S. Dresselhaus, Appl. Phys. Lett. **60**, 2204 (1992).

11) L. Chen, H. Ye and Y. Gogotsi, J. Am. Ceram. Soc. **87**, 147 (2004).

12) R. Y. Tay, H. Li, S. H. Tsang, L. Jing, D. Tan, M. Wei and E. H. T. Teo, Chem. Mater. **27**, 7156 (2015).

13) H. Suzuki, M. Kishibuchi, K. Shimogami, M. Maetani, K. Nasu, T. Nakagawa, Y. Tanaka, H. Inoue and Y. Hayashi, ACS Appl. Electron. Mater. **3**, 3555 (2021).

14) S. Furusawa, Y. Nakanishi, Y. Yomogida, Y. Sato, Y. Zheng, T. Tanaka, K. Yanagi, K. Suenaga, S. Maruyama, R. Xiang and Y. Miyata, ACS Nano **16**, 16636 (2022).

15) K. Li, G. Eres, J. Howe, Y.-J. Chuang, X. Li, Z. Gu, L. Zhang, S. Xie and Z. Pan, Sci. Rep. **3**, 2353 (2013).

16) X. Lin, W. Zhao, W. Zhou, P. Liu, S. Luo, H. Wei, G. Yang, J. Yang, J. Cui, R. Yu, L. Zhang, J. Wang, Q. Li, W. Zhou, W. Zhao, S. Fan and K. Jiang, ACS Nano **11**, 1257 (2017).

17) E. Loginova, N. C. Bartelt, P. J. Feibelman and K. F. McCarty, New J. Phys. **10**, 093026 (2008).
18) H. Kim, C. Mattevi, M. R. Calvo, J. C. Oberg, L. Artiglia, S. Agnoli, C. F. Hirjibehedin, M. Chhowalla and E. Saiz, ACS Nano **6**, 3614 (2012).
19) L. Ci, L. Song, C. Jin, D. Jariwala, D. Wu, Y. Li, A. Srivastava, Z. F. Wang, K. Storr, L. Balicas, F. Liu and P. M. Ajayan, Nat. Mater. **9**, 430 (2010).
20) W. Han, Y. Bando, K. Kurashima and T. Sato, Appl. Phys. Lett. **73**, 3085 (1998).
21) M. W. Smith, K. C. Jordan, C. Park, J.-W. Kim, P. T. Lillehei, R. Crooks and J. S. Harrison, Nanotechnology **20**, 505604 (2009).
22) A. L. Tiano, L. Gibbons, M. Tsui, S. I. Applin, R. Silva, C. Park and C. C. Fay, Nanoscale **8**, 4348 (2016).
23) P. Wang, Y. Zheng, T. Inoue, R. Xiang, A. Shawky, M. Watanabe, A. Anisimov, E. I. Kauppinen, S. Chiashi and S. Maruyama, ACS Nano **14**, 4298 (2020).
24) S. Maruyama, R. Kojima, Y. Miyauchi, S. Chiashi and M. Kohno, Chem. Phys. Lett. **360**, 229 (2002).
25) Y. Miyata, K. Kamon, K. Ohashi, R. Kitaura, M. Yoshimura and H. Shinohara, Appl. Phys. Lett. **96**, 263105 (2010).
26) C. Wei, R. Negishi, Y. Ogawa, M. Akabori, Y. Taniyasu and Y. Kobayashi, Jpn. J. Appl. Phys. **58**, SIIB04 (2019).
27) R. Negishi, C. Wei, Y. Yao, Y. Ogawa, M. Akabori, Y. Kanai, K. Matsumoto, Y. Taniyasu and Y. Kobayashi, Phys. status solidi **257**, 1900437 (2020).
28) Y. Yao, R. Negishi, D. Takajo, M. Takamura, Y. Taniyasu and Y. Kobayashi, Nanotechnology **33**, 155603 (2022).
29) T. S. Cheng, A. Davies, A. Summerfield, Y. Cho, I. Cebula, R. J. A. Hill, C. J. Mellor, A. N. Khlobystov, T. Taniguchi, K. Watanabe, P. H. Beton, C. T. Foxon, L. Eaves and S. V. Novikov, J. Vac. Sci. Technol. B **34**, 02L101 (2016).
30) A. C. Ferrari and J. Robertson, Phys. Rev. B **61**, 14095 (2000).
31) A. Eckmann, A. Felten, I. Verzhbitskiy, R. Davey and C. Casiraghi, Phys. Rev. B **88**, 035426 (2013).
32) L. Gustavo Cançado, M. Gomes da Silva, E. H. Martins Ferreira, F. Hof, K. Kampioti, K. Huang, A. Pénicaud, C. Alberto Achete, R. B. Capaz and A. Jorio, 2D Mater. **4**, 025039 (2017).
33) Q. Yuan, Z. Xu, B. I. Yakobson and F. Ding, Phys. Rev. Lett. **108**, 245505 (2012).
34) A. Summerfield, A. Davies, T. S. Cheng, V. V. Korolkov, Y. Cho, C. J. Mellor, C.

T. Foxon, A. N. Khlobystov, K. Watanabe, T. Taniguchi, L. Eaves, S. V. Novikov and P. H. Beton, Sci. Rep. **6**, 22440 (2016).

Figure Captions

Fig. 1. (a) Optical images of a BNNT film template suspended over a ring-shaped substrate (top) and the sample after the graphene growth (bottom). The right schematics show the corresponding nanostructures of a pristine BNNT and a BNNT coated with graphene. (b) STEM image and (c) EELS mapping of the few-layer graphene grown on a BNNT at 1350 °C. The EELS mapping shows the intensities of B *K*, N *K*, and C *K*-edge peaks and their composite.

Fig. 2. Raman spectra of the samples (a) grown at different temperatures for 5 min and (c) grown at 1350 °C for different growth times. (b) Growth temperature dependence and (d) growth time dependence of A_D/A_G (black circle, left axis) and Γ_G (red triangle, right axis).

Fig. 3. FTIR spectra of BNNT films before and after graphene growth.

Fig. 4. (a) B *K*-edge XANES spectra of BNNT films before and after graphene growth. (b) B *K*, C *K*, and N *K*-edge regions of electron energy loss spectra of a BNNT partially covered with graphene measured at different positions: bare BNNT without graphene and graphene grown on the BNNT.

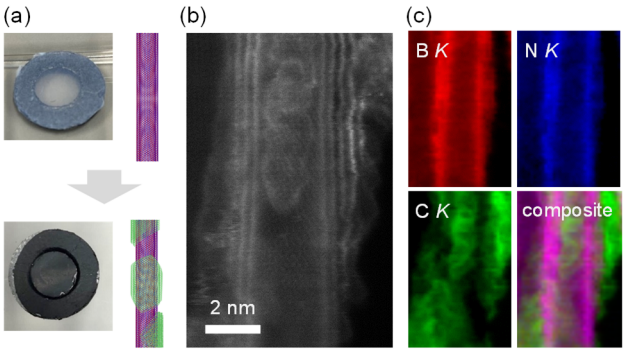

Fig. 1.

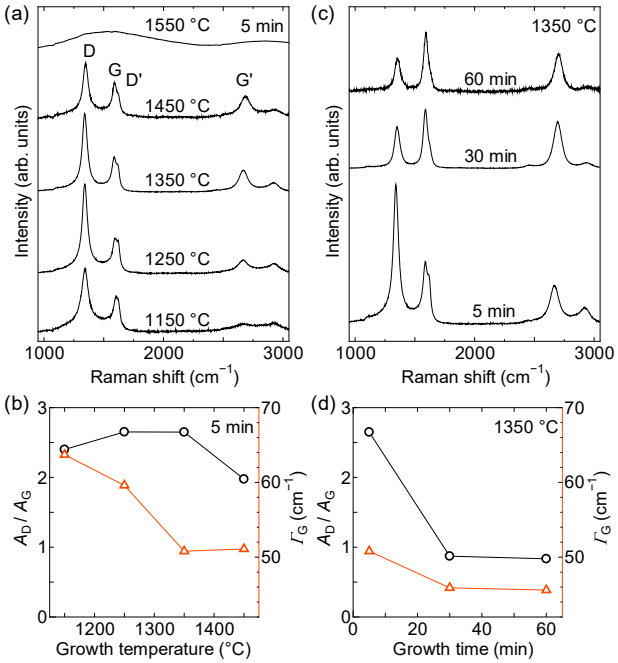

Fig. 2.

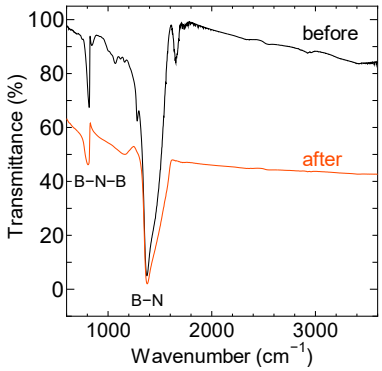

Fig. 3.

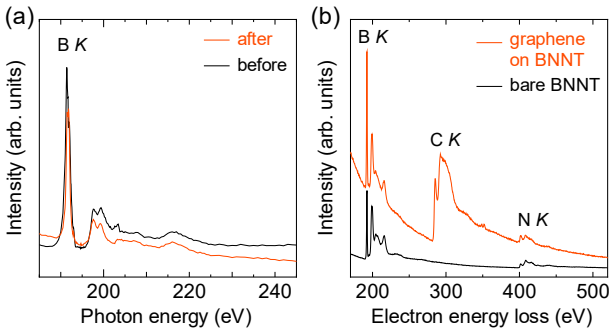

Fig. 4.

Supplementary data for

Coaxial heterostructure formation of highly crystalline graphene flakes on boron nitride nanotubes by high-temperature chemical vapor deposition

Masakiyo Kato[1], Taiki Inoue[1]*, Yi Ling Chiew[2], Yungkai Chou[1], Masashi Nakatake[3], Shoichi Takakura[3,4], Yoshio Watanabe[3], Kazu Suenaga[2,5], Yoshihiro Kobayashi[1]

[1]*Department of Applied Physics, Osaka University, Osaka 565-0871, Japan*

[2]*The Institute of Scientific and Industrial Research (ISIR-SANKEN), Osaka University, Osaka 567-0047, Japan*

[3]*Aichi Synchrotron Radiation Center, Aichi Science & Technology Foundation, Aichi 489-0985, Japan*

[4]*Synchrotron Radiation Research Center, Nagoya University, Aichi 464-8603, Japan*

[5]*Nanomaterials Research Institute, National Institute of Advanced Industrial Science and Technology (AIST), Tsukuba 305-8565, Japan*

E-mail: inoue.taiki@ap.eng.osaka-u.ac.jp

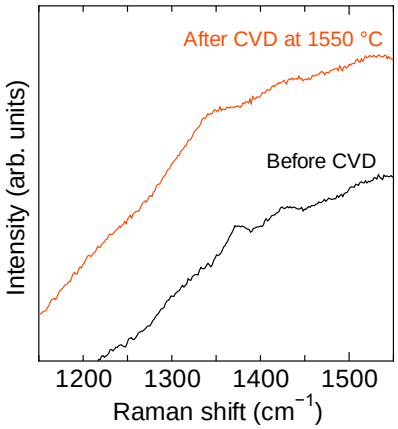

Fig. S1. Raman spectra of BNNT films before ethanol CVD (black) and after ethanol CVD at 1550 °C (red, same spectrum as Fig. 2(a)).

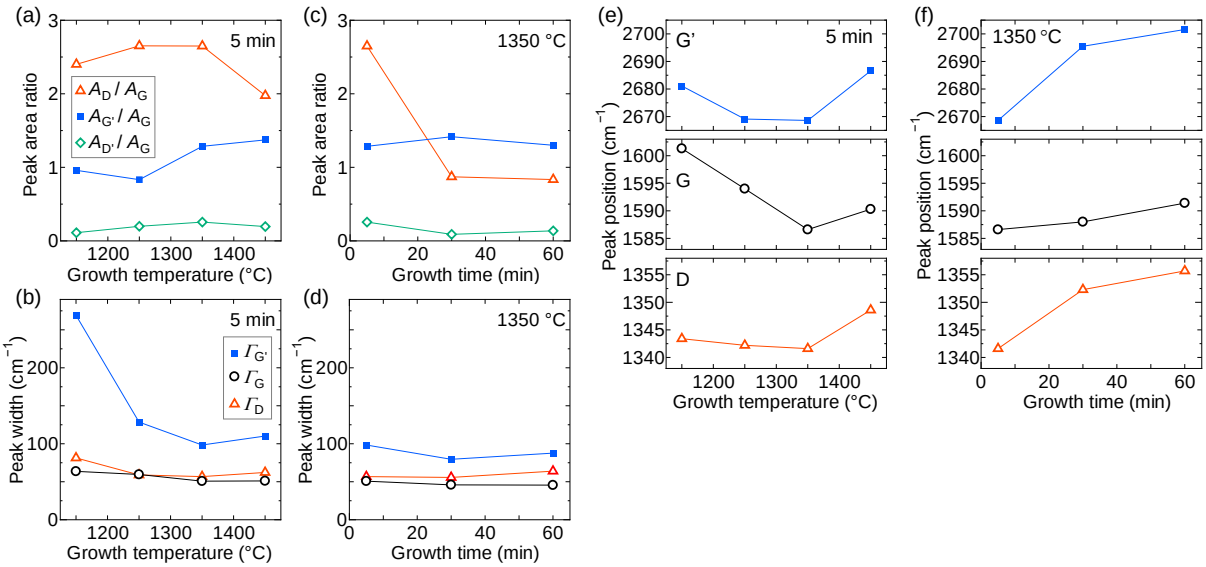

Fig. S2. Raman spectral features of graphene grown on the BNNT templates. (a,b,e) Growth temperature dependence with the fixed growth time of 5 min. (c,d,f) Growth time dependence with the fixed growth temperature at 1350 °C. (a,c) Peak intensity ratios A_D/A_G, $A_{G'}/A_G$, and $A_{D'}/A_G$. (b,d) Peak widths $\Gamma_{G'}$, Γ_G, and Γ_D. (e,f) Peak positions of G', G, and D bands.